Supporting Information For

"Structurally Robust Quaterphenyl-Dicarbonitrile 2D MOF Nanopores on Cu(111) for Cobalt Spin-Coordination Motifs"

Haruki Ishii[1], Kohei Tada[2,3], Ryo Ichikawa[1], Meng-Che Tsai[4], Kuei-Cheng Chen[4], Ryunosuke Sagehashi[5], Fumi Nishino[5], Keisuke Fukutani[5], Rikuya Hirota[2], Yasutaka Kitagawa[2,3], Satoshi Kera[5], Masaki Horie[4,6], and Toyo Kazu Yamada[1,7*]

1. Department of Materials Science, Chiba University, 1-33 Yayoi-Cho, Inage-ku, Chiba 263-8522, Japan.

2. Department of Materials Engineering Science, Graduate School of Engineering Science, The University of Osaka, Toyonaka, Osaka 560-8531, Japan

3 Innovative Catalysis Science Division, Institute for Open and Transdisciplinary Research Initiatives (ICS-OTRI), The University of Osaka, Suita, Osaka 565-0871, Japan

4. Department of Chemical Engineering, National Tsing Hua University, 101, Sec. 2, Kuang-Fu Road, Hsinchu, 30013, Taiwan

5 Institute for Molecular Science, Myodaiji, Okazaki 444-8585 Japan

6. Research Institute for Electronic Science, Hokkaido University, N21W10, Kita-Ward, Sapporo 001-0021, Japan

7. Molecular Chirality Research Centre, Chiba University, 1-33 Yayoi-cho, Inage-ku, Chiba 263-8522, Japan.

Author Information,

*Corresponding Author: Toyo Kazu Yamada, E-mail: toyoyamada@faculty.chiba-u.jp

Version 2026.3.30

Figure S1

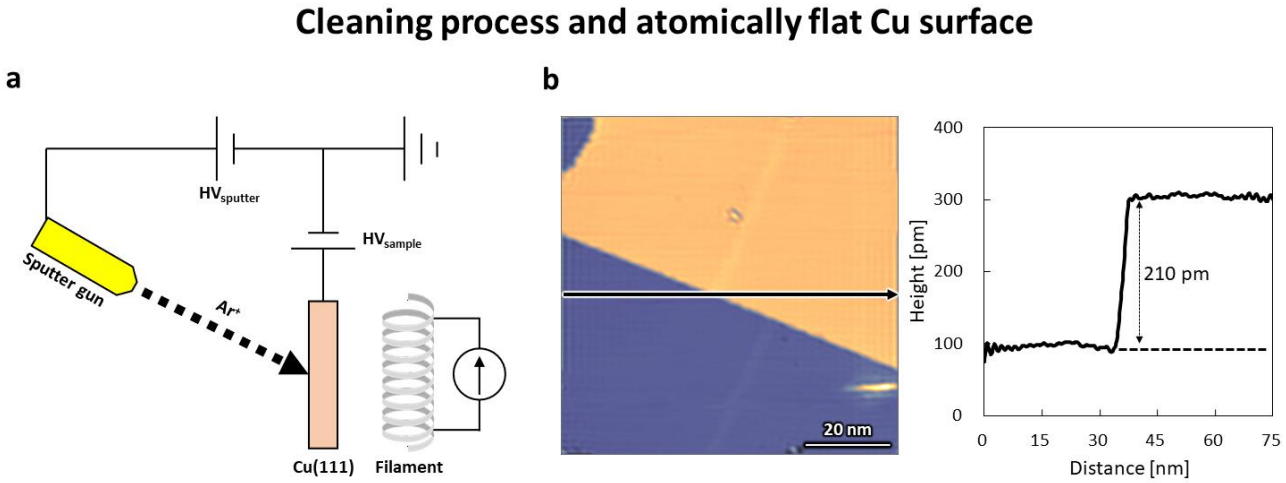

Figure S1. (a) Schematic of the sputtering–annealing cycle used for Cu(111) surface preparation. (b) STM topographic image of the cleaned Cu(111) surface (80 × 80 nm^2, -2 V, 300 pA). The line profile reveals a step height of approximately 210 pm, consistent with a single atomic step of Cu(111).

Figure S2

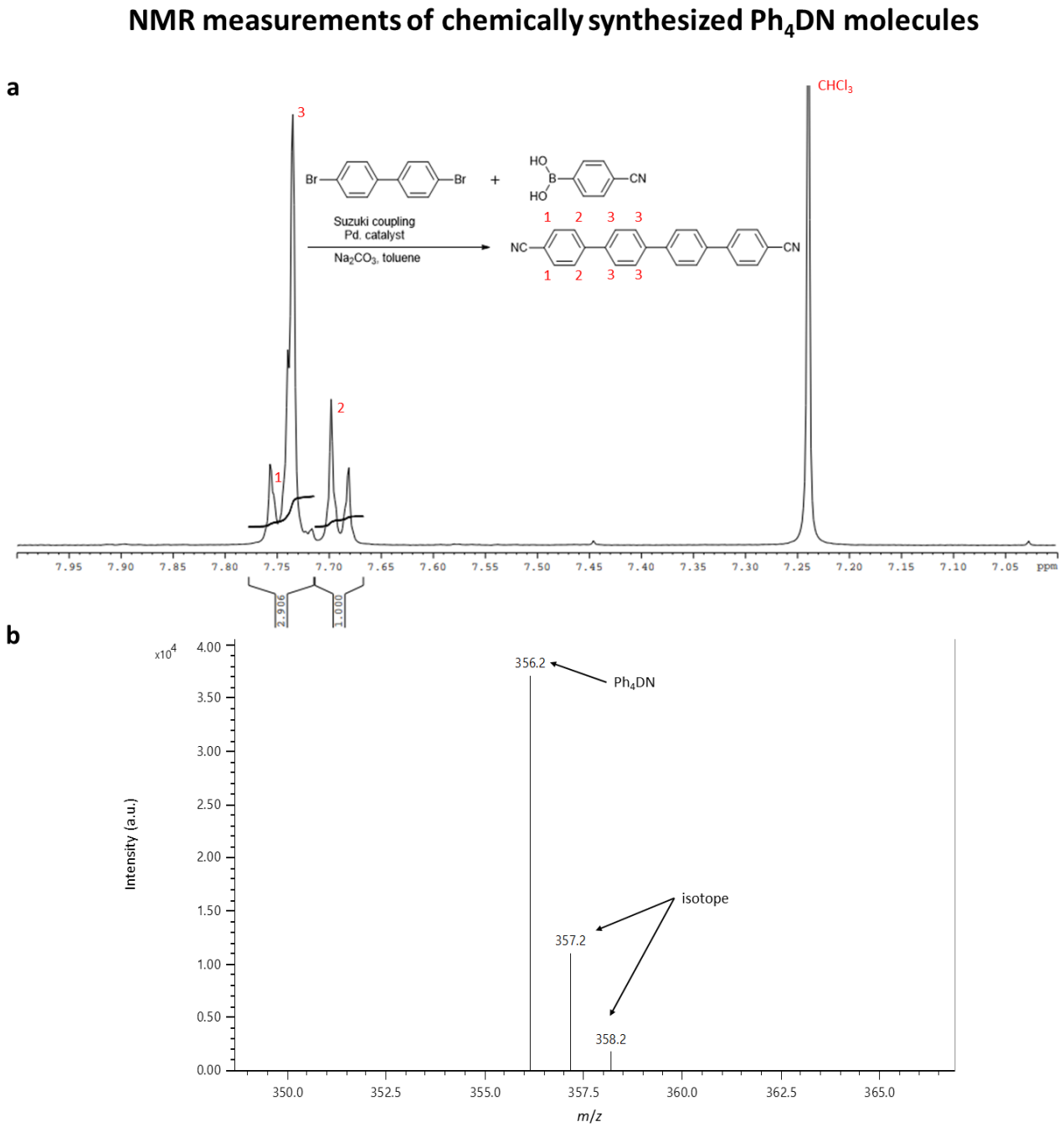

Figure S2. (a) ^{1}H NMR spectrum of Ph_4DN (500MHz, $CDCl_3$): δ(ppm) = 7.75 (d, J = 9.0 Hz, 4H), 7.74 (s, 8H), 7.69 (d, J = 8.5 Hz, 4H). (b) Low-resolution field desorption mass spectrum of Ph_4DN. The peak at m/z = 356.2 corresponds to $[C_{26}H_{16}N_2]^+$ = 356.13.

Figure S3

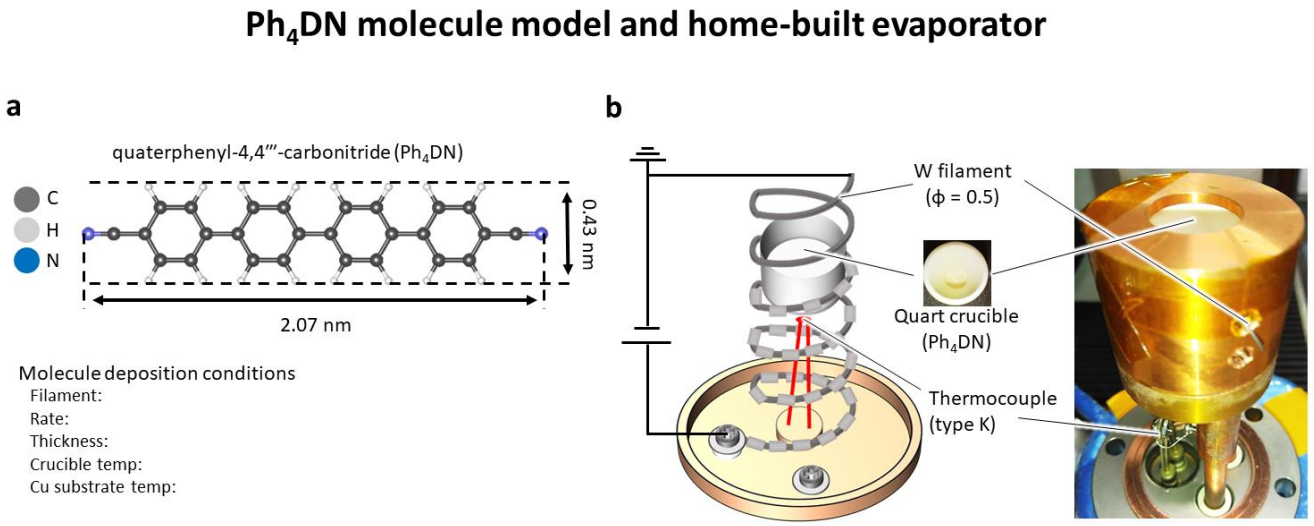

Figure S3. (a) Molecular structure of Ph_4DN and deposition conditions. (b) Schematic illustration and photo image of the molecular evaporator.

Figure S4

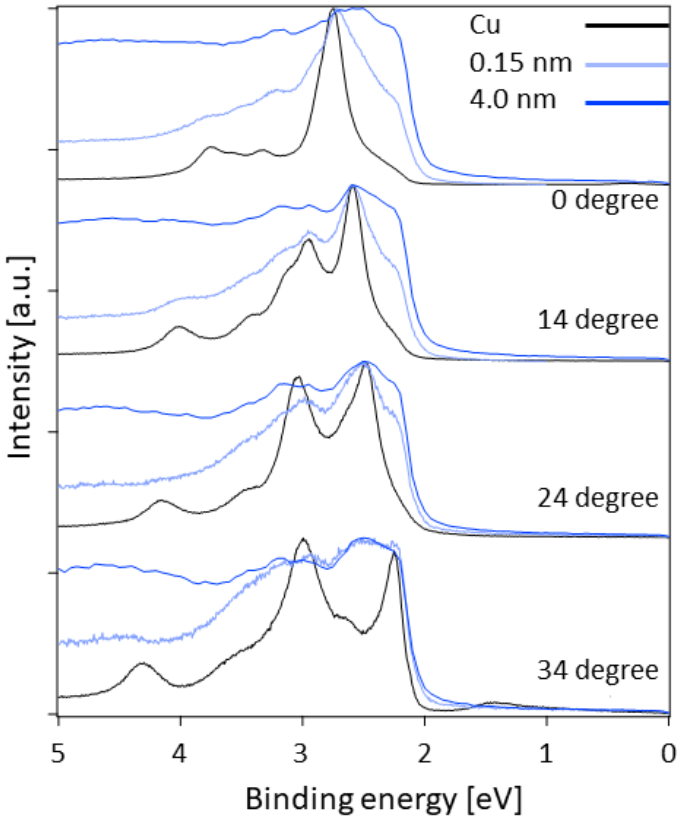

Figure S4. ARPES spectra at different emission angles for bare Cu(111), 0.15 nm Ph_4DN, and 4.0 nm Ph_4DN on Cu(111).

Figure S5

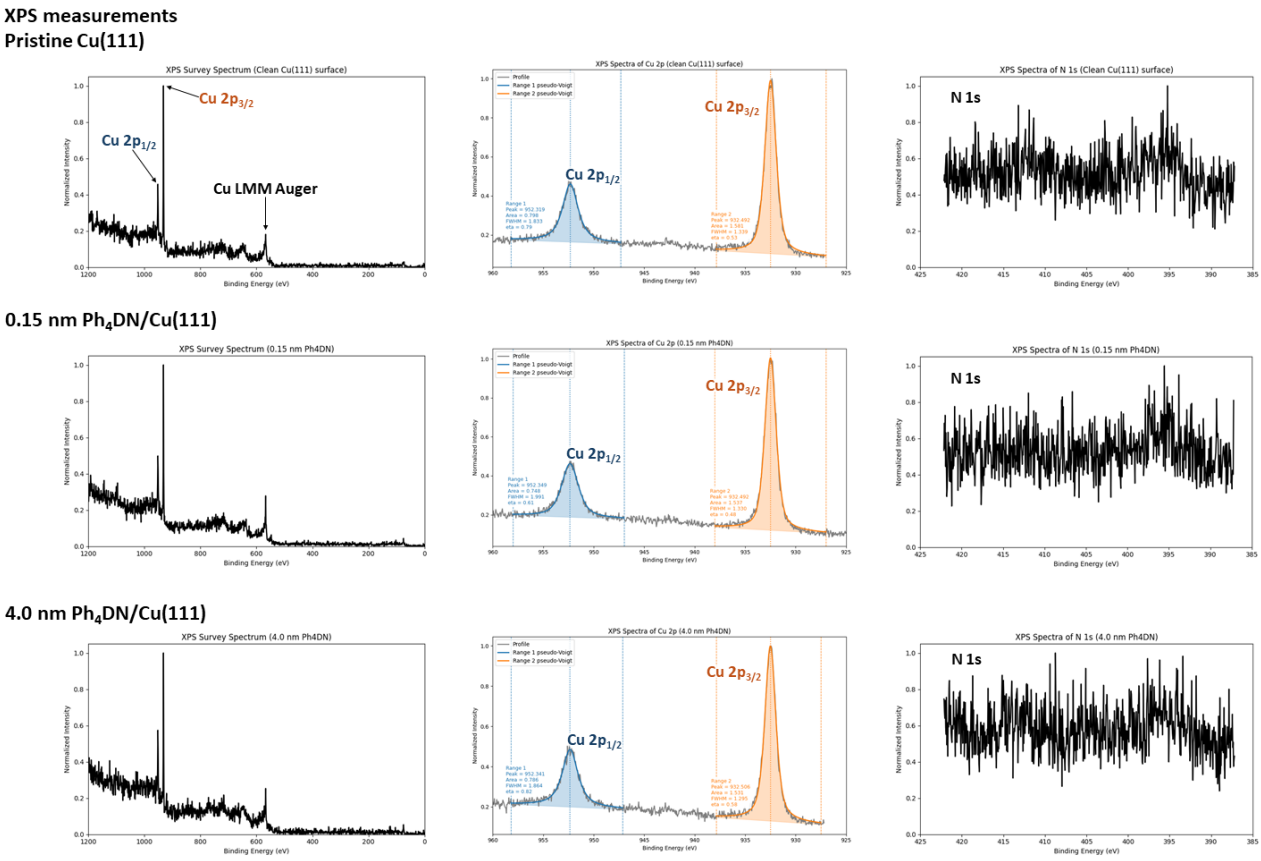

Figure S5. XPS measurements for bare Cu(111) (top row), 0.15 nm Ph_4DN (middle row), and 4.0 nm Ph_4DN (bottom row) on Cu(111), where the binding energy regions of Cu 2*p* and N 1*s* are measured (middle and right panels). The Cu 2*p* spectra show no discernable change upon the MOF formation and N 1*s* are likely under the detection limit in this measurement.

Supplementary Note 1 for the Comparison of DFT and PFP

DFT calculations were conducted to evaluate the predictive accuracy of the machine-learned interatomic potential (MLIP) used in this study, PFP [1]. The exchange-correlation functional was treated using the generalized gradient approximation (GGA) with the Perdew–Burke–Ernzerhof (PBE) formulation [2]. A plane-wave basis set was employed to construct the wave functions, and core electrons were described using the projector augmented-wave (PAW) method [3,4]. The number of valence electrons was set to 11 for Cu, 5 for N, 4 for C, and 1 for H. The energy cutoffs for the wave function and the augmented charge density were 400 eV and 2400 eV, respectively. Atomic charges were estimated using the Bader analysis based on the electron density obtained from the DFT calculations [5–8]. All calculations were performed using a single Γ-point. The DFT calculations were carried out with the VASP code [9–12].

Figure S6 presents the results of geometry optimization performed without the Cu(111) surface. The initial structure, shown in Fig. S6a, is an ideal honeycomb lattice. Both DFT and PFP calculations yielded optimized structures in which the Ph_4DN molecules adopt a three-dimensionally distorted configuration with noticeable twisting. In the PFP-optimized structure, the molecules exhibit more pronounced twisting compared to the DFT result and lie relatively closer to a flat plane. Despite minor differences between the DFT and PFP results, the initially ideal 2D network underwent significant distortion during the optimization process. Furthermore, the number of valence electrons for Cu in the optimized structures was approximately 10, with no significant

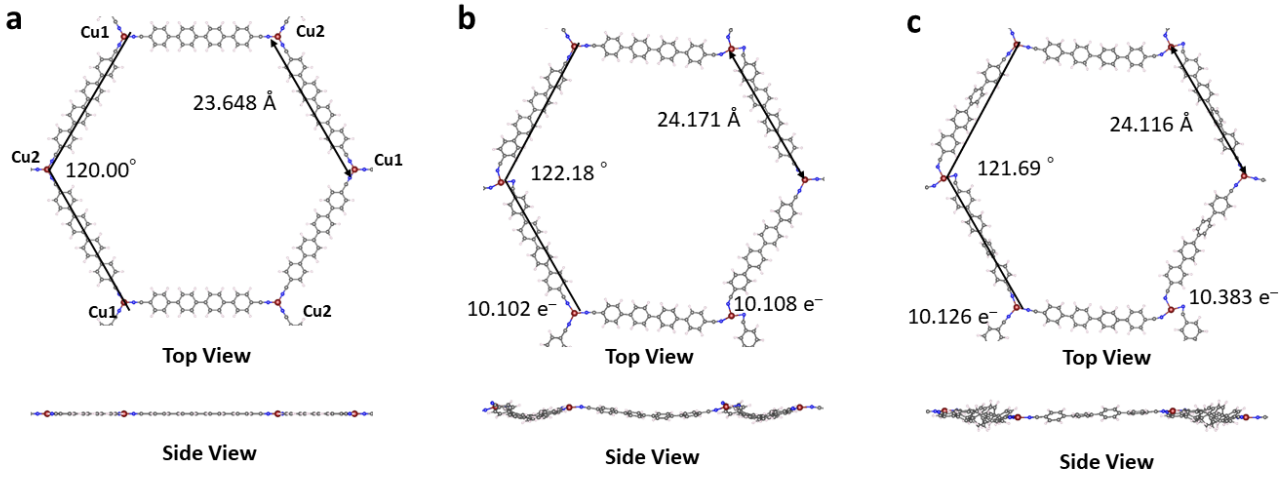

Figure S6. (a) Initial structure of Cu-Ph_4DN MOF, and optimized structures by (b) DFT and (c) PFP. The valence electron numbers are also shown.

difference observed between the DFT and PFP calculations.

To assess the accuracy of energy estimation for models including the Cu substrate, the interaction energy between Cu(111) and the 2D MOF was compared. The Cu(111) surface was modeled as a monoatomic layer, and the structures of both the Cu(111) and 2D MOF were kept fixed. Figure S7 shows the calculated potential energy curves, clearly demonstrating that the PFP method accurately reproduces the DFT results for the 2D MOF on Cu(111).

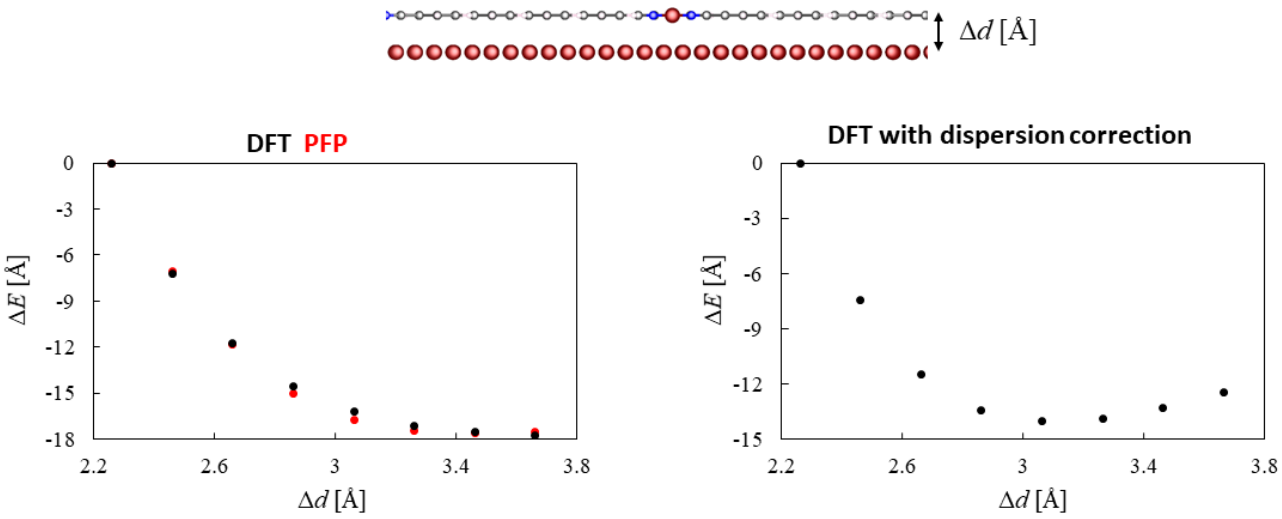

Figure S7. Total energy difference (ΔE) from the model structure, where the distance between Cu-Ph_4DN and Cu(111) is 2.26 Å. The results of DFT (black dots) and PFP (red dots) are in good agreement. The results shown in the left panel do not include any dispersion force correction, i.e., the CRYSTAL_U0 mode and pure PBE functional were used for PFP and DFT, respectively.

(1) Takamoto, S.; Shinagawa, C.; Motoki, D.; Nakago, K.; Li, W.; Kurata, I.; Watanabe, T.; Yayama, Y.; Iriguchi, H.; Asano, Y.; Onodera, T.; Ishii, T.; Kudo, T.; Ono, H.; Sawada, R.; Ishitani, R.; Ong, M.; Yamaguchi, T.; Kataoka, T.; Hayashi, A.; Charoenphakdee, N.; Ibuka, T. Towards Universal Neural Network Potential for Material Discovery Applicable to Arbitrary Combination of 45 Elements. *Nat Commun* **2022**, *13* (1), 2991. https://doi.org/10.1038/s41467-022-30687-9.

(2) Perdew, J. P.; Burke, K.; Ernzerhof, M. Generalized Gradient Approximation Made Simple. *Phys. Rev. Lett.* **1996**, *77* (18), 3865–3868. https://doi.org/10.1103/PhysRevLett.77.3865.

(3) Blöchl, P. E. Projector Augmented-Wave Method. *Phys. Rev. B* **1994**, *50* (24), 17953–17979. https://doi.org/10.1103/PhysRevB.50.17953.

(4) Kresse, G.; Joubert, D. From Ultrasoft Pseudopotentials to the Projector Augmented-Wave Method.

Phys. Rev. B **1999**, *59* (3), 1758–1775. https://doi.org/10.1103/PhysRevB.59.1758.

(5) Henkelman, G.; Arnaldsson, A.; Jónsson, H. A Fast and Robust Algorithm for Bader Decomposition of Charge Density. *Computational Materials Science* **2006**, *36* (3), 354–360. https://doi.org/10.1016/j.commatsci.2005.04.010.

(6) Sanville, E.; Kenny, S. D.; Smith, R.; Henkelman, G. Improved Grid-based Algorithm for Bader Charge Allocation. *J Comput Chem* **2007**, *28* (5), 899–908. https://doi.org/10.1002/jcc.20575.

(7) Tang, W.; Sanville, E.; Henkelman, G. A Grid-Based Bader Analysis Algorithm without Lattice Bias. *J. Phys.: Condens. Matter* **2009**, *21* (8), 084204. https://doi.org/10.1088/0953-8984/21/8/084204.

(8) Yu, M.; Trinkle, D. R. Accurate and Efficient Algorithm for Bader Charge Integration. *The Journal of Chemical Physics* **2011**, *134* (6), 064111. https://doi.org/10.1063/1.3553716.

(9) Kresse, G.; Hafner, J. *Ab Initio* Molecular Dynamics for Liquid Metals. *Phys. Rev. B* **1993**, *47* (1), 558–561. https://doi.org/10.1103/PhysRevB.47.558.

(10) Kresse, G.; Hafner, J. *Ab Initio* Molecular-Dynamics Simulation of the Liquid-Metal–Amorphous-Semiconductor Transition in Germanium. *Phys. Rev. B* **1994**, *49* (20), 14251–14269. https://doi.org/10.1103/PhysRevB.49.14251.

(11) Kresse, G.; Furthmüller, J. Efficient Iterative Schemes for *Ab Initio* Total-Energy Calculations Using a Plane-Wave Basis Set. *Phys. Rev. B* **1996**, *54* (16), 11169–11186. https://doi.org/10.1103/PhysRevB.54.11169.

(12) Kresse, G.; Furthmüller, J. Efficiency of Ab-Initio Total Energy Calculations for Metals and Semiconductors Using a Plane-Wave Basis Set. *Computational Materials Science* **1996**, *6* (1), 15–50. https://doi.org/10.1016/0927-0256(96)00008-0.

Figure S8

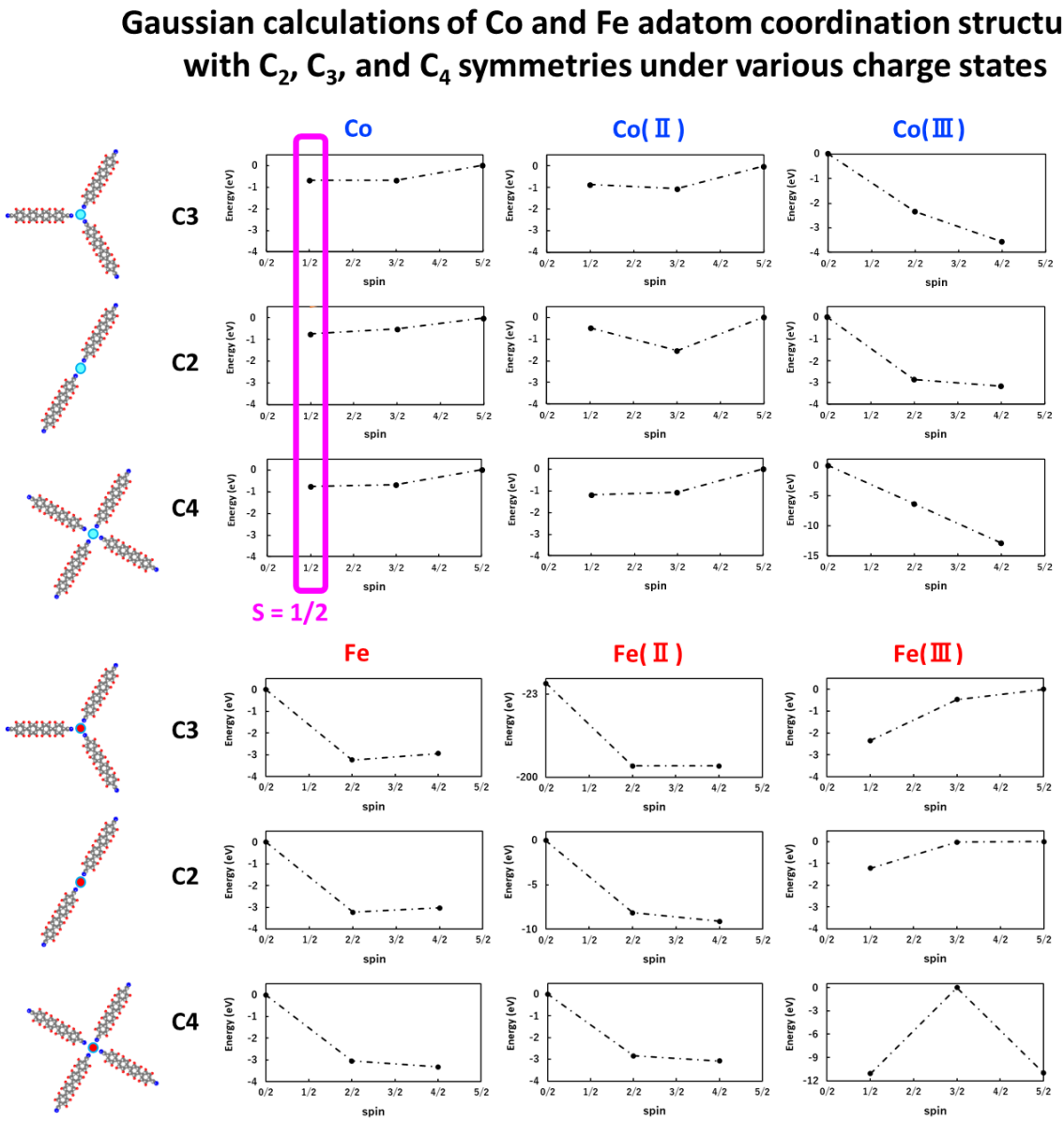

Figure S8. Relative energy differences calculated using DFT (Gaussian 16) for Ph_4DN coordination to Co and Fe atoms with C_2, C_3, and C_4 symmetries. The used functional and basis sets were B3LYP and SDDALL, respectively. The effective core potentials for the SDDALL were used.

Supplementary Note 2

We initially investigated a shorter linear precursor composed of three benzene rings, 1,4-Di(4-pyridyl)benzene (DPB), and observed the formation of a 2D MOF on a Cu(111) surface. However, the DPB molecules primarily formed C_2-symmetric linear chains and a self-assembled monolayer (SAM) without well-defined nanopores (see Supplementary, Fig. S9). Furthermore, DPB began to sublimate at approximately 320 K under UHV, just above room temperature, making it difficult to achieve a consistent and controllable deposition rate.

Figure S9

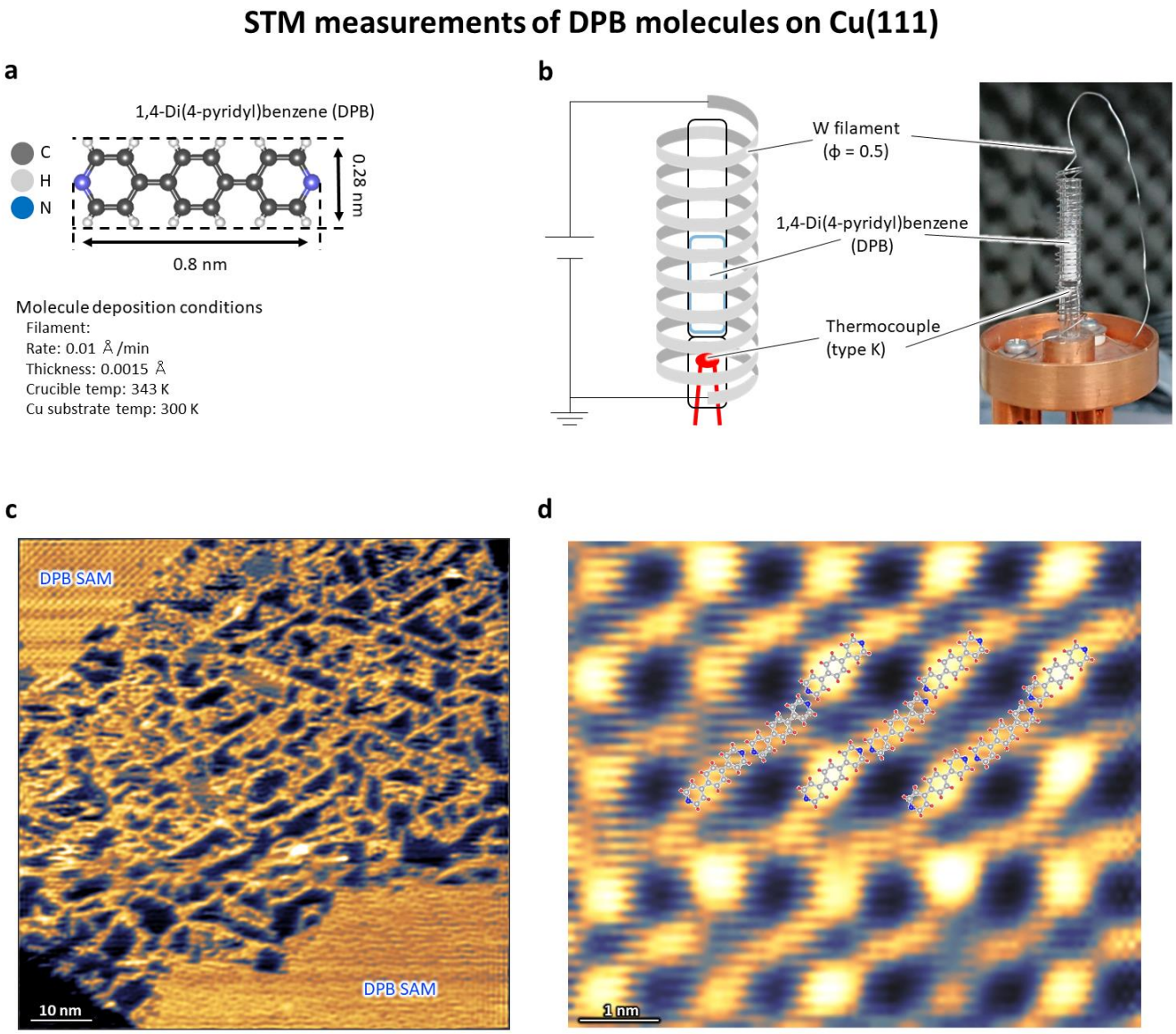

Figure S9. (a) Molecular structure of the DPB molecule and deposition conditions. (b) Schematic illustration and photo image of our home-built molecular evaporator. (c) STM topographic image of the DPB molecules on Cu(111), in which 2D SAM area and one-dimensional networks are observed (80 × 80 nm^2, -2.0 V, 50 pA). (d) Magnified STM topographic image of DPB SAM structure on Cu(111) (7.3 × 6.2 nm^2, -2.0 V, 100 pA).

Figure S10

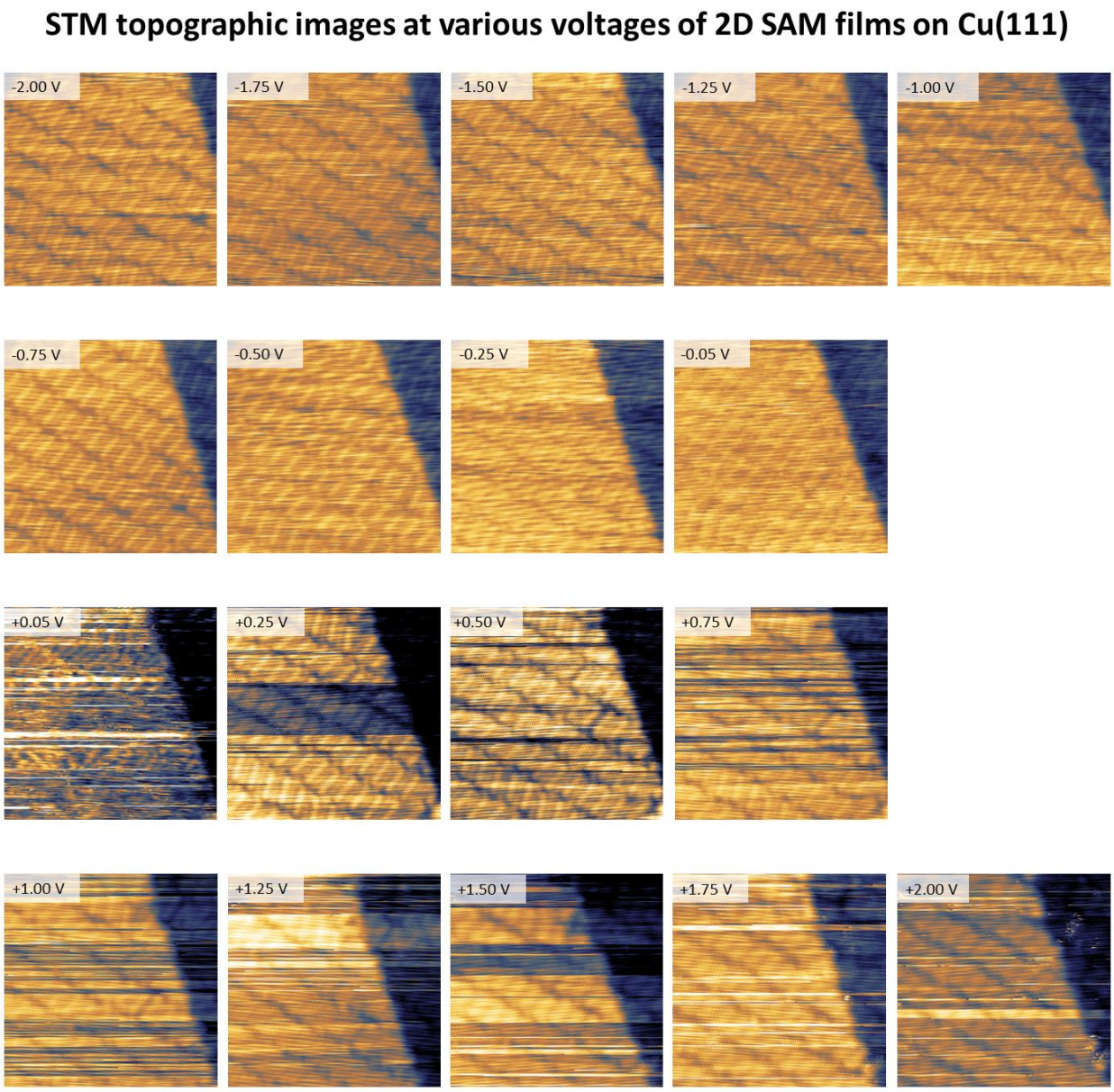

Figure S10. STM topographic images (14 × 14 nm^2, I_t = 50 pA) of the Ph_4DN SAM region at various sample bias voltages between -2 V and +2 V. Within the HOMO-LUMO gap, the molecular patterns are not clearly visible.

Figure S11

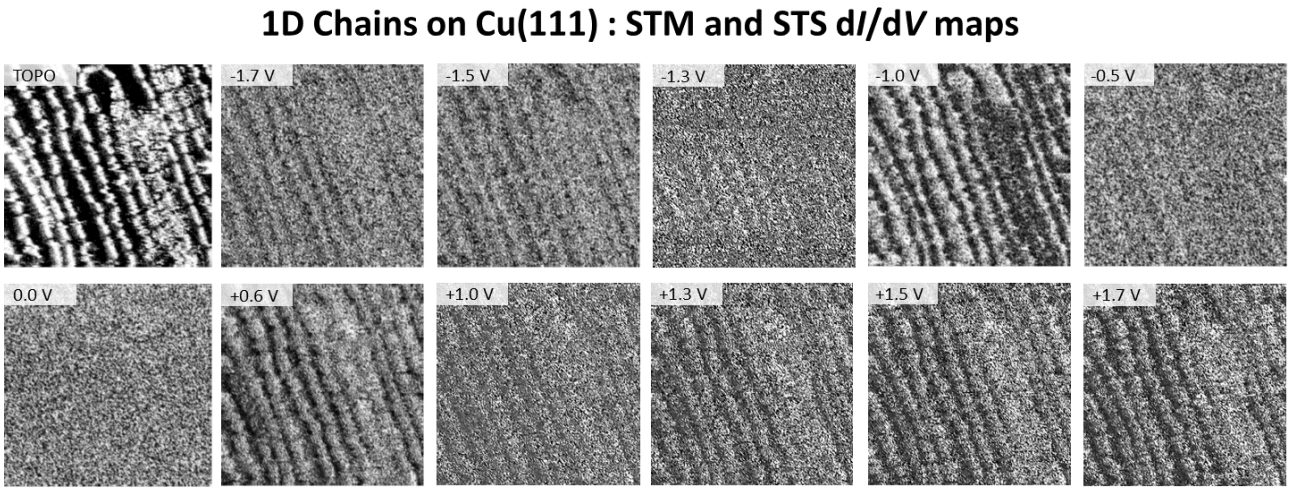

Figure S11. Scanning tunneling spectroscopy mapping on the 1D chain area of Ph_4DN / Cu(111), where simultaneously obtained STM topographic image (20 × 20 nm^2, -1.8 V, 50 pA) and d*I*/d*V* maps at -1.7, -1.5, -1.3, -1.0, -0.5, 0.0, +0.6, +1.0, +1.3, +1.5, and +1.7 V.

Figure S12

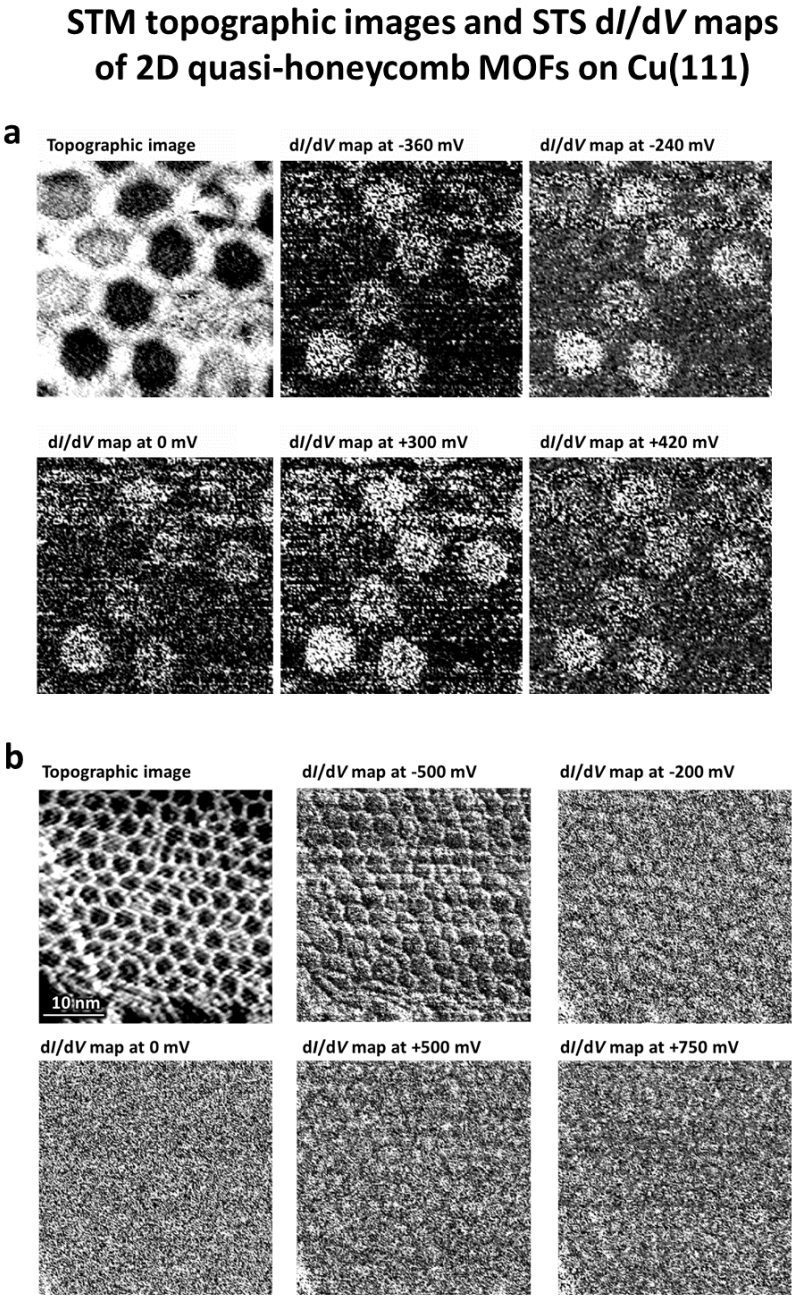

Figure S12. Electronic structures of the 2D quasi-honeycomb networks on Cu(111). (a) STM topographic image (14 × 14 nm^2, -0.75 V, 50 pA) and simultaneously obtained dI/dV maps at -360, -240, 0, +300, and +420 mV. (b) STM topographic image (40 × 40 nm^2, -0.75 V, 50 pA) and simultaneously obtained dI/dV maps at -500, -200, 0, +500, and +750 mV.

Figure S13

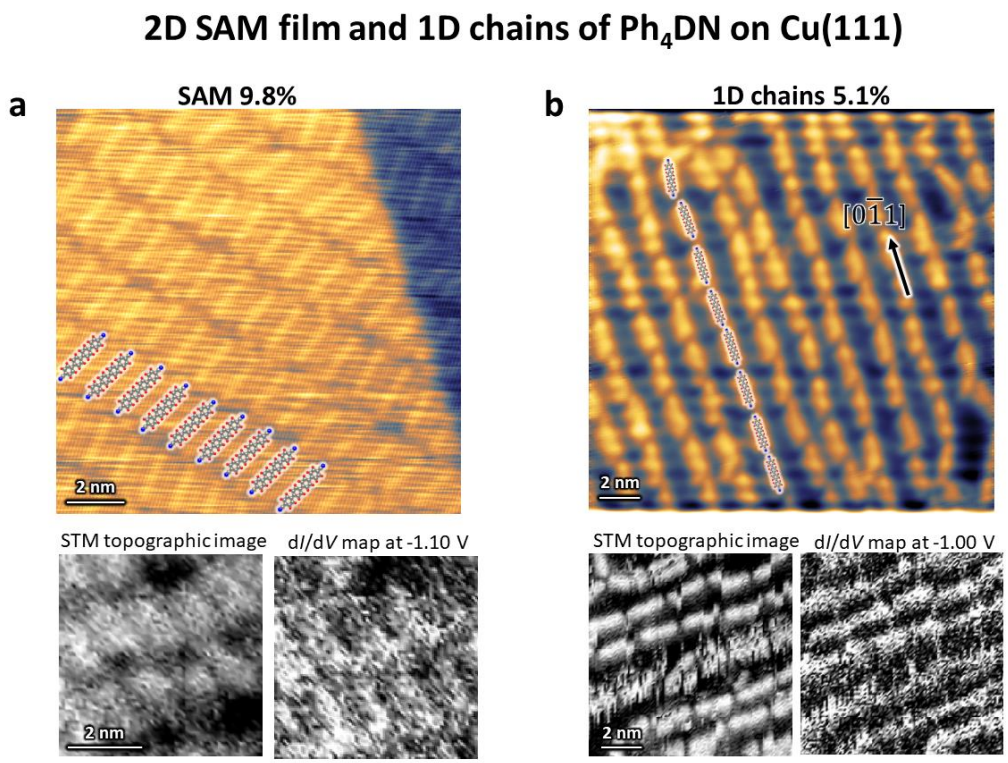

Figure S13. (a) STM topographic image of Ph_4DN SAM array (14 × 14 nm^2, V_s = -1.0 V, I_t = 50 pA), and the magnified STM image and the simultaneously obtained dI/dV map at -1.1 V (lower panels, 6 × 6 nm^2). (b) STM topographic image of Ph_4DN 1D chains (20 × 20 nm^2, 20 pA, -1.8 V), and the magnified STM image and the simultaneously obtained dI/dV map at -1.0 V (lower panels, 10 × 10 nm^2).

Figure S14

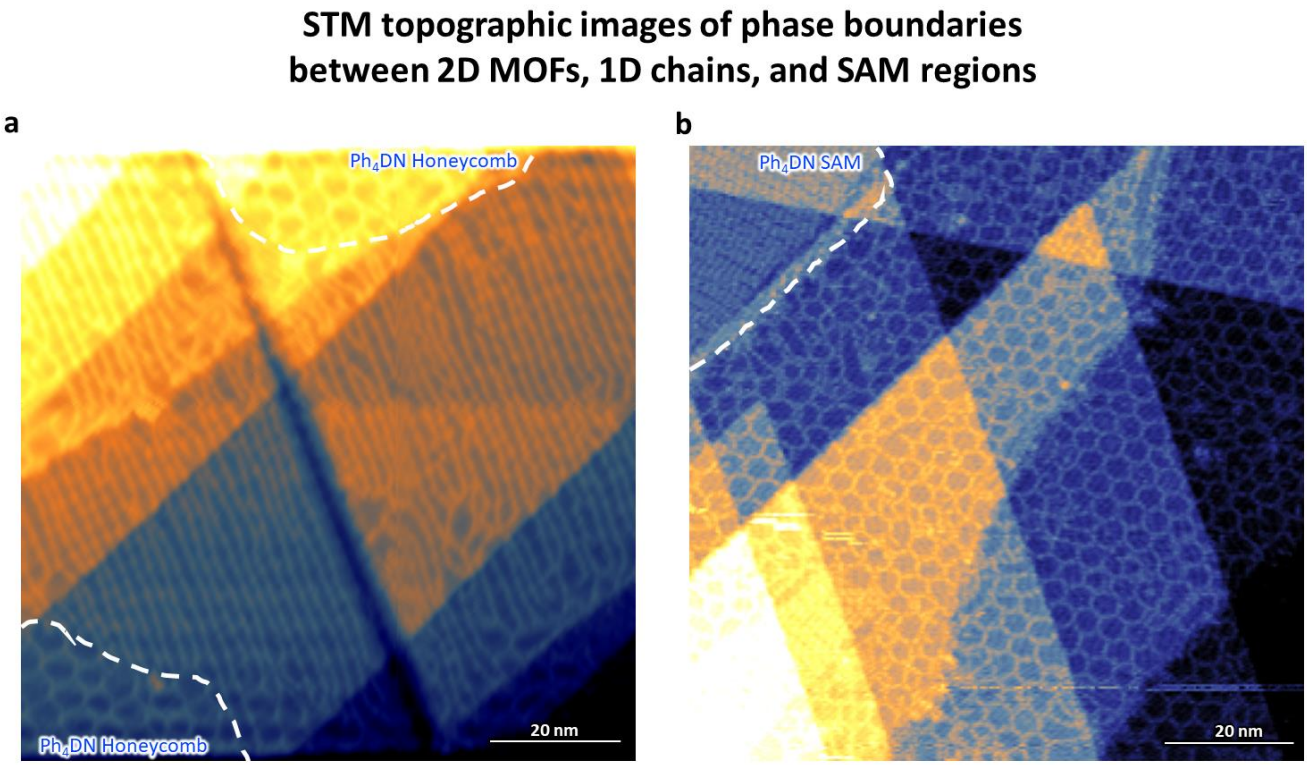

Figure S14. STM topographic images (78 K) obtained on Cu(111) after the Ph_4DN deposition in UHV at 300 K. In (a), a two-dimensional honeycomb network region coexists with a one-dimensional chain region, and the two merge at their boundary (80 × 80 nm^2, -1.8 V, 50 pA). In (b), the honeycomb network transitions smoothly into the SAM region (95 × 95 nm^2, 0.75 V, 50 pA).

Figure S15

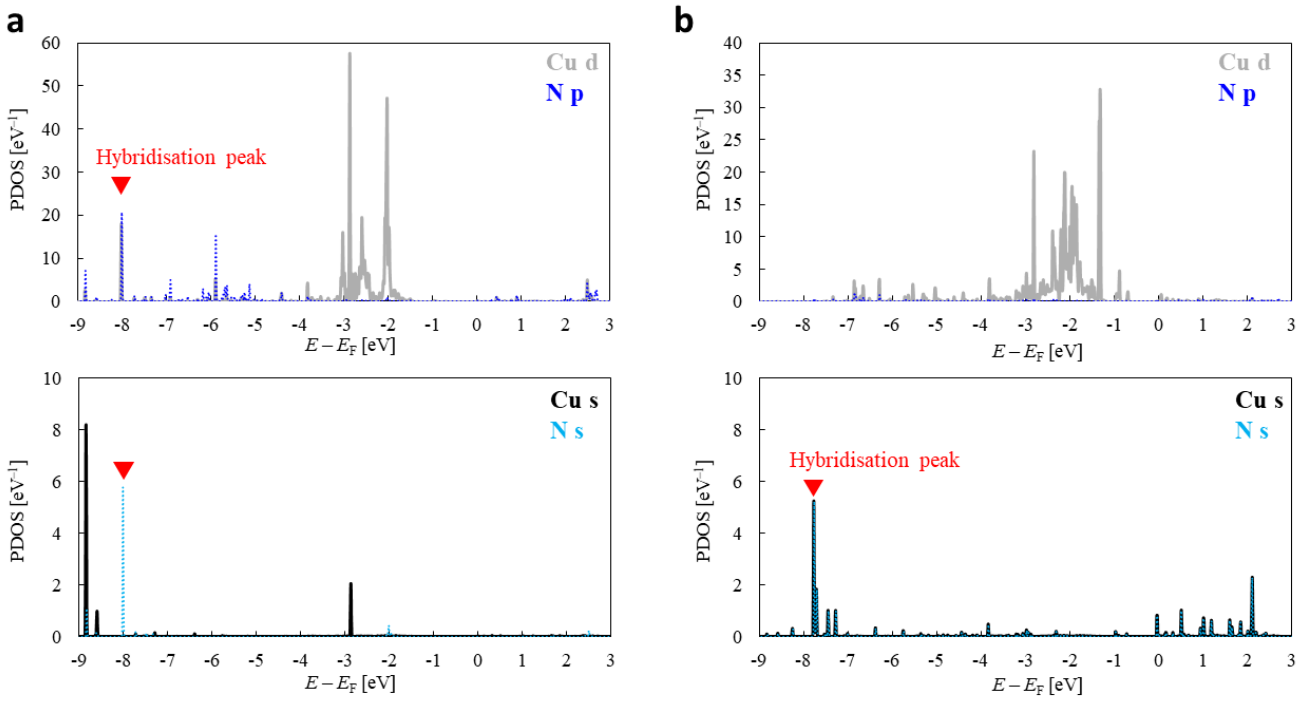

Figure S15. Projected density of states (PDOS) of the 2D MOF on Cu(111) model whose structure was optimised by MLIP and shown in Fig. 1d. (a) PDOS results of Cu in C_3 junction and coordinated N, and (b) those of Cu in chiral junction and coordinated N. E_F represents the Fermi energy of calculated model. Upper panels show the components of Cu 3*d* and N 2*p*, while lower panels show those of Cu 4*s* and N 2*s*. We found Cu 3*d* bands at -1.5 < $E - E_F$ < -3.5 eV, and hybridisation peaks between Cu and N. For C_3 junction (a), Cu 3*d*, N 2*s*, and N 2*p* are hybridised and the corresponding peak is found at $E - E_F$ = -8 eV, while for chiral junction, Cu 4*s* and N 2*s* hybridisation is found at $E - E_F$ = -7.8 eV.

Figure S16

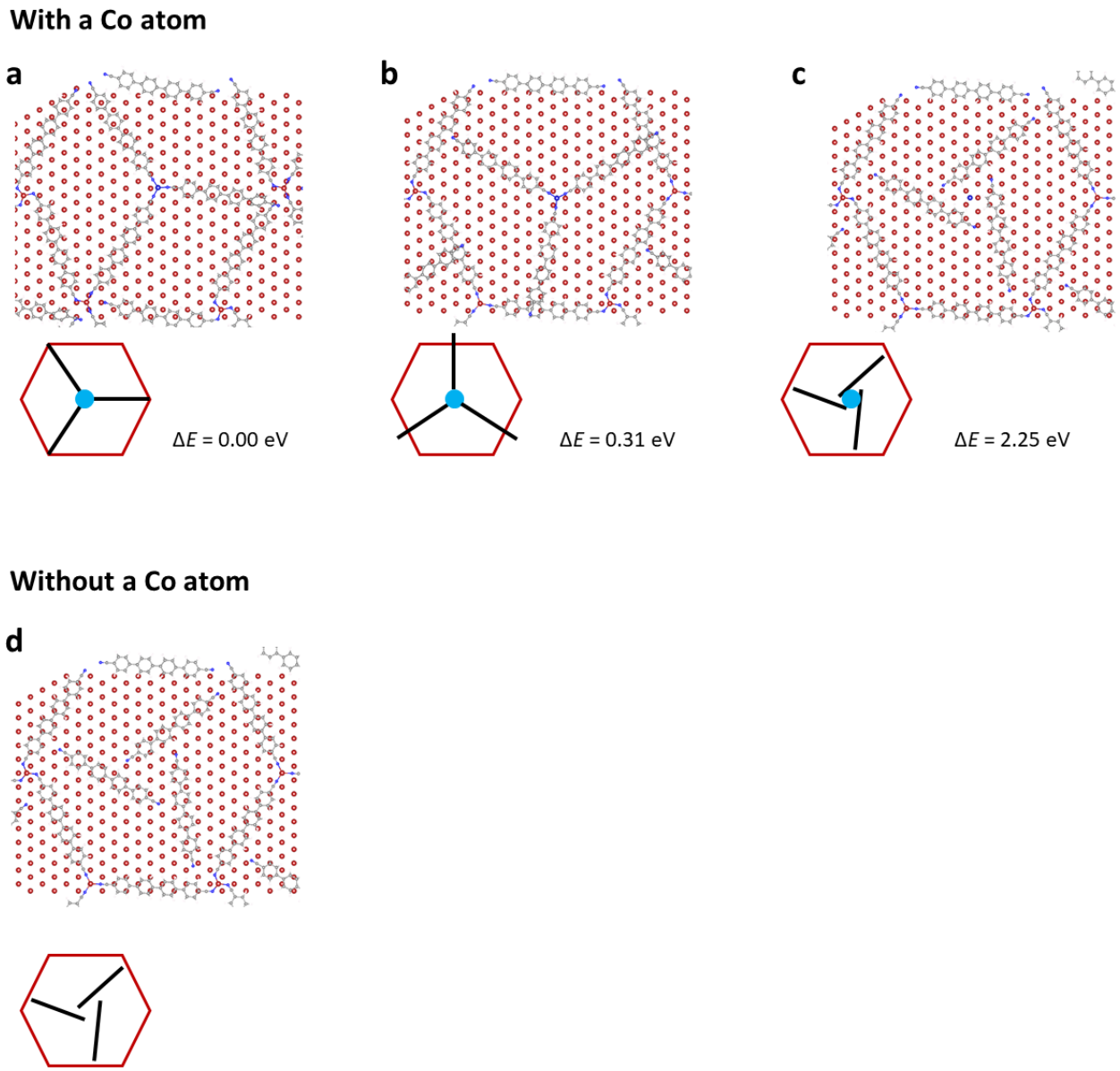

Figure S16. Optimized structures of additional Ph_4DN models (a–c) with a Co adatom and (d) without. Brown hexagons represent schematic views. ΔE denotes the energy difference of each Co-adatom model relative to its most stable configuration.